AIAA JOURNAL
Vol. 39, No. 8, August 2001

Experimental and Theoretical Study on Aeroelastic Response of High-Aspect-Ratio Wings

Deman Tang* and Earl H. Dowell†
Duke University, Durham, North Carolina 27708-0300

An experimental high-aspect-ratio wing aeroelastic model with a slender body at the tip has been constructed, and the response due to flutter and limit-cycle oscillations (LCO) has been measured in a wind-tunnel test. A theoretical model has been developed and calculations made to correlate with the experimental data. Structural equations of motion based on nonlinear beam theory are combined with the ONERA aerodynamic stall model to study the effects of geometric structural nonlinearity and steady angle of attack on flutter and LCO of high-aspect-ratio wings. Static deformations in the vertical and torsional directions caused by a steady angle of attack and gravity are measured, and results from theory and experiment are compared. A dynamic perturbation analysis about a nonlinear static equilibrium is used to determine the small perturbation flutter boundary, which is compared to the experimentally determined flutter velocity and oscillation frequency. Time simulation is used to compute the LCO response. The results between the theory and experiment are in good agreement for static aeroelastic response, the onset of flutter, and dynamic LCO amplitude and frequency.

Nomenclature

C_d = section drag coefficient
C_l = section lift coefficient
C_m = section torsional moment coefficient
C_ξ = structural damping
$c, \bar{c}$ = wing chord and dimensionless chord, c/L
c_{SB} = chord of slender body
$\mathrm{d}D$, $\mathrm{d}L$ = section drag and lift forces
$\mathrm{d}F_v$, $\mathrm{d}F_w$ = section chordwise and vertical component forces
$\mathrm{d}M_x$ = section pitch moment about elastic axis
$\mathrm{d}M_0$ = section pitch moment about one-quarter chord
E = modulus of elasticity
e = section mass center from elastic axis
G = shear modulus
g = gravitational constant
I_1, I_2 = vertical, chordwise area moments
J = torsional stiffness constant
K_m = wing mass radius of gyration
L = wing span
M = tip mass of the wing
m = mass per unit length of the wing
N = total number of modes
NN = number of aerodynamic elements
t = time
U = freestream velocity
V_j, W_j = generalized coordinates for bending
v = chordwise or edgewise bending deflection
w = vertical or flapwise bending deflection
x = position coordinate along wing span
$y_{\mathrm{a.c.}}$ = distance of aerodynamic center of airfoil section from elastic axis
α_l = wing section angle of attack
Δ_l = dimensionless width of lth spanwise aerodynamic element
θ_0 = steady angle of attack at root section
ρ = air density
Φ_j = generalized coordinates for torsion
ϕ = twist about deformed elastic axis
ω_{vj} = jth chordwise natural frequency of wing
ω_{wj} = jth vertical natural frequency of wing
$\omega_{\phi j}$ = jth torsional natural frequency of wing
$'$ = $\mathrm{d}/\mathrm{d}x$
$\dot{}$ = $\mathrm{d}/\mathrm{d}t$

Introduction

AEROELASTIC stability and response of an aircraft with a high-aspect-ratio wing, from subsonic to supersonic flow, have been studied for many years. Most investigators have used linear beam theory to simplify the wing structural model. As shown in Refs. 1–3, however, a geometric structural nonlinearity may arise from the coupling between elastic flap or vertical bending, chordwise or edgewise bending, and torsion for very high-aspect-ratio wings typical of uninhabited air vehicles (UAV). In Refs. 2 and 3, the effect of the large static preflutter deformation on the flutter boundary and limit-cycle oscillation (LCO) response has been studied. The results provide additional insight with respect to the contribution of structural nonlinear coupling to the aeroelastic stability and response of high-aspect-ratio wings. Flap or vertical bending refers to bending perpendicular to the wing chord, and chordwise or edgewise bending refers to bending in the direction parallel to the wing chord.

An experimental high-aspect-ratio wing aeroelastic model with a tip mass has been constructed and a wind-tunnel test conducted to measure the static aeroelastic response, flutter, and LCO. The goal is to assess experimentally the theoretical results of earlier studies.[2,3] The theoretical structural equations of motion are based on nonlinear beam theory[1] and the original ONERA aerodynamic stall model.[4] Large static preflutter deformations in the vertical or torsional direction are created by the gravity loading on the wing and a tip slender body, as well as a steady angle of attack, which creates a static aerodynamic load on the wing.

A dynamic perturbation equation about a nonlinear static equilibrium is derived that is used to determine the flutter boundary. A direct time-marching solution is also used to calculate the large-amplitude response behavior of this nonlinear system both above and below the nominal, perturbation flutter boundary, that is, the flutter boundary determined from the dynamic equations linearized about a nonlinear static equilibrium state.

Before the wind-tunnel test, a static and vibration test of the experimental model has been made and the results compared to the theoretical predictions. Also, we use the present theoretical method to correlate with an earlier experiment conducted by Dowell et al.[5] A discussion of these latter results and correlation with the measured data are given in the Appendix.

Received 18 September 2000; revision received 21 December 2000; accepted for publication 16 January 2001.

*Research Associate Professor, Department of Mechanical Engineering and Materials Science. Member AIAA.

†J. A. Jones Professor, Department of Mechanical Engineering and Materials Science. Fellow AIAA.

This paper is a complement to the studies reported earlier by Patil et al.,[2,6] by Patil and Hodges,[7] by Tang and Dowell,[3] and by Dowell et al.[5]

Experimental Wing Model and Measurements

The experimental model includes two parts: a high-aspect-ratio wing with a slender body at the tip and a root support mechanism. The wing is rectangular, untwisted, and flexible in the flap, lag, and torsional directions. The wing is constructed from a precision ground flat steel spar with mass uniformly distributed along the wingspan. The spar is 45.72 cm in length, 1.27 cm in width, and 0.127 cm in thickness. It is inserted tightly into the wing root mechanism. To reduce torsional stiffness, the spar has multiple thin flanges along the span. The flange width is 0.127 cm, and it is 0.318 cm deep. There are 2 × 33 flanges uniformly and symmetrically distributed along the wingspan and centerline of the spar. There are 18 pieces of NACA 0012 airfoil plate uniformly distributed along the span. The pieces of the airfoil plate are made of aluminum alloy with 0.254-cm thickness. A precision aerodynamic contour of the wing model is obtained. Each airfoil plate has a slot 1.27 cm in width and 0.127 cm in thickness at the symmetry line. The spar is inserted through these airfoil plate slots, and they are permanently bonded together. Each space between two airfoil plates is filled with a light wood (bass) covering the entire chord and span, which provides the aerodynamic contour of the wing. This wood provides a slight additional mass and a small addition to the bending and torsion stiffness.

A slender body is attached to the elastic axis of the wing tip. The slender body is an aluminum bar, 0.95 cm in diameter and 10.16 cm in length. A paraboloidal forebody and an aftbody with 1.14-cm length are fixed to two ends of the bar. The forebody and aftbody are made of brass. The geometry of the paraboloidal forebody is described as follows:

$$R/R_0 = \bar{y}^2, \qquad \bar{y} = 0 \rightarrow 1$$

The slender body is symmetrical and is designed to provide enough torsional inertia to reduce the natural torsional frequency sufficiently to induce flutter in the velocity range of the wind tunnel.

A physical representation of wing model is shown in Fig. 1.

The root support mechanism is a socket that allows a change of the steady angle of attack at the root. The root socket is mounted to the midpoint of side wall of the wind tunnel as shown in Fig. 2, which is a photograph of the aeroelastic wing model in the wind tunnel.

Axial strain gauges for bending modes and a 45-deg oriented strain gauge for torsional modes were glued to the root spar to measure the bending–torsional deflections of the wing. Signals from the strain gauges were conditioned and amplified before their measurement through a gauge conditioner and a low-pass filter. A microaccelerometer is mounted at the midspan of the wing. The output signals from these transducers are directly recorded on a computer with data acquisition and analysis software, Lab-VIEW 5.1.

A helium–neon laser with 0.8 MW randomly polarized and wavelength 633 (nm) is mounted on the top of the tunnel. The top of the tunnel is made of a glass plate with a thickness of 1.27 cm. A mirror, 1.27 cm in diameter, is fixed on the tip of the wing. A mirror deflection technique is used to determine the geometric twist angle and the vertical or flapwise bending slope at the wing tip.

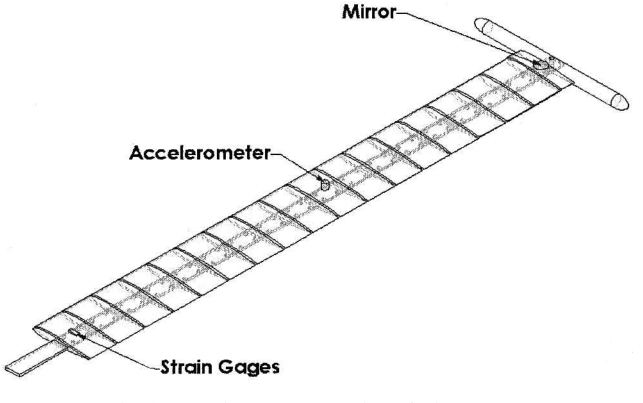

Fig. 1 Physical representation of wing model.

Table 1 Experimental wing model data

Property	Value
Wing	
Span L	0.4508 m
Chord c	0.0508 m
Mass per unit length	0.2351 kg/m
Moment of inertia (50% chord)	0.2056×10^{-4} kgm
Spanwise elastic axis	50% chord
Center of gravity	49% chord
Flap bending rigidity EI_1	0.4186 Nm^2
Chordwise bending rigidity EI_2	0.1844×10^2 Nm^2
Torsional rigidity GJ	0.9539 Nm^2
Flap structural modal damping ξ_w	0.02
Chordwise structural modal damping ξ_v	0.025
Torsional structural modal damping ξ_ϕ	0.031
Slender body	
Radius R	0.4762×10^{-2} m
Chord length c_{SB}	0.1406 m
Mass M	0.0417 kg
Moment of inertia I_x	0.9753×10^{-4} kgm^2
Moment of inertia I_y	0.3783×10^{-5} kgm^2
Moment of inertia I_z	0.9753×10^{-4} kgm^2

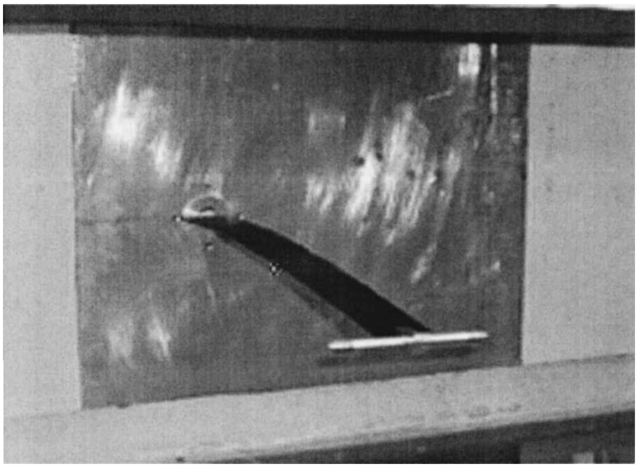

Fig. 2 Photograph of experimental model in wind tunnel.

All static, flutter, and LCO response tests were performed in the Duke University low-speed wind-tunnel. The wind tunnel is a closed-circuit tunnel with a test section of 0.7×0.53 m^2 and a length of 1.52 m. The maximum air speed attainable is 89.3 m/s.

The basic parameters of the experimental wing model were obtained from standard static and vibration tests and are listed in Table 1.

Nonlinear and Perturbation Flutter Equations

Structural Model

According to the Hodges–Dowell equations[1] for a uniform, untwisted elastic wing, neglecting cross-sectional warping, the equations of motion may be written as

$$\begin{aligned} &EI_2 v'''' + (EI_2 - EI_1)[\phi(w)'']'' + m\ddot{v} + C_\xi \dot{v} \\ &\quad + (M\ddot{v} + I_v \ddot{v}')\delta(x - L) = \frac{\mathrm{d}F_v}{\mathrm{d}x} + \Delta F_v \\ &\quad - [Mg\delta(x - L) + mg]\sin\theta_0 \end{aligned} \tag{1}$$

$$\begin{aligned} &EI_1(w)'''' + (EI_2 - EI_1)(\phi v'')'' + m\ddot{w} - me\ddot{\phi} + C_\xi \dot{w} \\ &\quad + (M\ddot{w} + I_w \ddot{w}')\delta(x - L) = \frac{\mathrm{d}F_w}{\mathrm{d}x} + \Delta F_w \\ &\quad - [Mg\delta(x - L) + mg]\cos\theta_0 \end{aligned} \tag{2}$$

$$-GJ\phi'' + (EI_2 - EI_1)w''v'' + I_\phi\ddot{\phi}\delta(x-L) + mK_m^2\ddot{\phi}$$

$$+ C_\xi\dot{\phi} - me\ddot{w} = \frac{\mathrm{d}M_x}{\mathrm{d}x} + \Delta M_x \tag{3}$$

A few general comments about Eqs. (1–3) may be in order. First, by the multiplication of each of these equations by δv, δw, and $\delta\phi$, respectively, and the integration over the length of the beam, a variational statement may be derived. Conversely, as shown in Ref. 1, these equations may be derived from Hamilton's principle.

Note that in Eqs. (1–3) only the most important nonlinear terms are retained from the Hodges–Dowell equations.[1] The third- and higher-order geometrically nonlinear terms are neglected here. Also note that the geometric twist angle

$$\hat{\phi} = \phi + \int_0^x v'w''\,\mathrm{d}x$$

is considered in the aerodynamic terms. M is the tip mass; I_v, I_w, and I_ϕ are the tip inertial terms; θ_0 is the pitch angle or steady angle of attack at the root of this wing model; and e is the distance between mass center and wing elastic axis center.

The aerodynamic forces include two parts. One contribution is from the wing surface, $\mathrm{d}F_w/\mathrm{d}x$, $\mathrm{d}F_v/\mathrm{d}x$, and $\mathrm{d}M_x/\mathrm{d}x$, and the other is from the slender body at the wing tip, ΔF_w, ΔF_v, and ΔM_x.

ONERA Aerodynamic Airfoil Model

The v and w components of the aerodynamic force and the aerodynamic moment about the elastic axis can be expressed as follows:

$$\mathrm{d}F_w = \mathrm{d}L - (\phi_\lambda - \theta_0)\,\mathrm{d}D, \qquad \mathrm{d}F_v = -\mathrm{d}D - (\phi_\lambda - \theta_0)\,\mathrm{d}L$$

$$\mathrm{d}M_x = \mathrm{d}M_0 - y_{\mathrm{a.c.}}\,\mathrm{d}F_w \tag{4}$$

where

$$\mathrm{d}L = \tfrac{1}{2}\rho c U^2 C_l\,\mathrm{d}x, \qquad \mathrm{d}D = \tfrac{1}{2}\rho c U^2 C_d\,\mathrm{d}x$$

$$\mathrm{d}M_0 = \tfrac{1}{2}\rho c^2 U^2 C_m\,\mathrm{d}x, \qquad \phi_\lambda \approx \dot{w}/(U + \dot{v} + \dot{w}\theta_0)$$

$$\alpha = \hat{\phi} + \theta_0 - \phi_\lambda$$

The section aerodynamic coefficients C_l, C_d, and C_m are obtained from the original ONERA stall aerodynamic model (see Refs. 4 and 8). These airfoil relationships are combined with a strip theory assumption to determine the wing aerodynamic forces. Patil and Hodges[7] have shown the strip theory assumption is a good one for such high-aspect-ratio wings.

Slender Body Theory

We follow Bisplinghoff et al. (Ref. 9, p. 418 et seq.) and provide their equation numbers. Using essentially the nomenclature of Ref. 9, we define $h = w_{x=L}$, $\alpha = \phi_{x=L}$, $L = \Delta F_w$, and $M_x = \Delta M_x$, but use the symbol y to denote chordwise position. Then the vertical displacement at the wing tip is

$$Z_a = -h - \alpha[y - y_B] \tag{5}$$

Eq. (7-136) from Ref. 9, where $y_B \equiv y_{\mathrm{ea}}$ is the distance from leading edge to the elastic axis of the slender body. Here h indicates positive up and α positive nose up. Now the downwash or convected vertical velocity is

$$W_a = \frac{\partial Z_a}{\partial t} + U\frac{\partial Z_a}{\partial y} = \frac{\mathrm{D}Z_a}{\mathrm{D}t} \tag{6}$$

Eq. (7-137) from Ref. 9, where $D \equiv \partial/\partial t + U(\partial/\partial y)$.

Thus, from Ref. 9, Eq. (7-140) is

$$\frac{\mathrm{d}L}{\mathrm{d}y} = -\rho\frac{\mathrm{D}S}{\mathrm{D}t} - \rho S\frac{\mathrm{D}^2 Z_a}{\mathrm{D}t^2} = -\rho\frac{\mathrm{D}}{\mathrm{D}t}\left[S\frac{\mathrm{D}Z_a}{\mathrm{D}t}\right] \tag{7}$$

where S is identical to the body cross-sectional area and $S = \pi R^2$ for a circular cross section of radius $R(y)$. Note that

$$\frac{\mathrm{D}S}{\mathrm{D}t} = U\frac{\mathrm{d}S}{\mathrm{d}y} \tag{8}$$

in Eq. (7-142) from Ref. 9. Then Eq. (7-140) becomes

$$\frac{\mathrm{d}L}{\mathrm{d}y} = -\rho U\frac{\mathrm{d}S}{\mathrm{d}y}\frac{\mathrm{D}Z_a}{\mathrm{D}t} - \rho S\frac{\mathrm{D}^2 Z_a}{\mathrm{D}t^2} \tag{9}$$

Eq. (7-143) from Ref. 9.

Now,

$$L \equiv \int_0^{c_{\mathrm{SB}}} \frac{\mathrm{d}L}{\mathrm{d}y}\,\mathrm{d}y$$

$$M_x \equiv \int_0^{c_{\mathrm{SB}}} \frac{\mathrm{d}L}{\mathrm{d}y}[y - y_B]\,\mathrm{d}y$$

where c_{SB} is identical to the chord of slender body.

Using Eq. (7-136) from Ref. 9 or Eq. (5),

$$\frac{\mathrm{D}Z_a}{\mathrm{D}t} = -\dot{h} - \dot{\alpha}[y - y_B] - U\alpha$$

$$\frac{\mathrm{D}^2 Z_a}{\mathrm{D}^2 t} = -\ddot{h} - \ddot{\alpha}[y - y_B] - 2U\dot{\alpha}$$

thus,

$$\Delta F_w = L \equiv \int_0^{c_{\mathrm{SB}}} \frac{\mathrm{d}L}{\mathrm{d}y}\,\mathrm{d}y = \rho[\ddot{h} + U\dot{\alpha}]\int_0^{c_{\mathrm{SB}}} S\,\mathrm{d}y$$

$$+ \rho\ddot{\alpha}\int_0^{c_{\mathrm{SB}}} S[y - y_B]\,\mathrm{d}y \tag{10}$$

$$\Delta M_x = M_x \equiv -\int_0^{c_{\mathrm{SB}}} \frac{\mathrm{d}L}{\mathrm{d}y}[y - y_B]\,\mathrm{d}y = \rho U[\dot{h} + U\alpha]\int_0^{c_{\mathrm{SB}}} S\,\mathrm{d}y$$

$$- \rho\ddot{h}\int_0^{c_{\mathrm{SB}}} S[y - y_B]\,\mathrm{d}y - \rho\ddot{\alpha}\int_0^{c_{\mathrm{SB}}} S[y - y_B]^2\,\mathrm{d}y \tag{11}$$

Note that

$$\int_0^{c_{\mathrm{SB}}} \frac{\mathrm{d}S}{\mathrm{d}y}\,\mathrm{d}y = -\int_0^{c_{\mathrm{SB}}} S\,\mathrm{d}y$$

if $S = 0$ at $y = 0$, c_{SB}, that is, for a pointed body.

Also, recall the sign convention is y-positive aft, L-positive up, and M_x-positive nose up.

If we assume the slender body drag can be neglected, then

$$\Delta F_v = -(\phi_\lambda - \phi - \theta_0)\Delta F_w \tag{12}$$

Modal Equations

Expansions in general mode shape functions are used to obtain ordinary differential equations in terms of generalized coordinates from Eqs. (1–3). They are expressed in series form as follows:

$$\bar{v} = \sum_{j=1}^{N} V_j(t)\psi_j(\bar{x}), \qquad \bar{w} = \sum_{j=1}^{N} W_j(t)\psi_j(\bar{x})$$

$$\phi = \sum_{j=1}^{N} \Phi_j(t)\Theta_j(\bar{x}) \tag{13}$$

where the overbar indicates nondimensionalization with respect to the wingspan L, and ψ_j and Θ_j are the jth normal modes of the associated linear structural model.

Let $\{q\}$ be a state vector, which is defined as

$$\{q\} = \{\dot{V}_j, V_j, \dot{W}_j, W_j, \dot{\Phi}, \Phi_j, C_{ll}, C_{ml}, C_{dl}\}$$

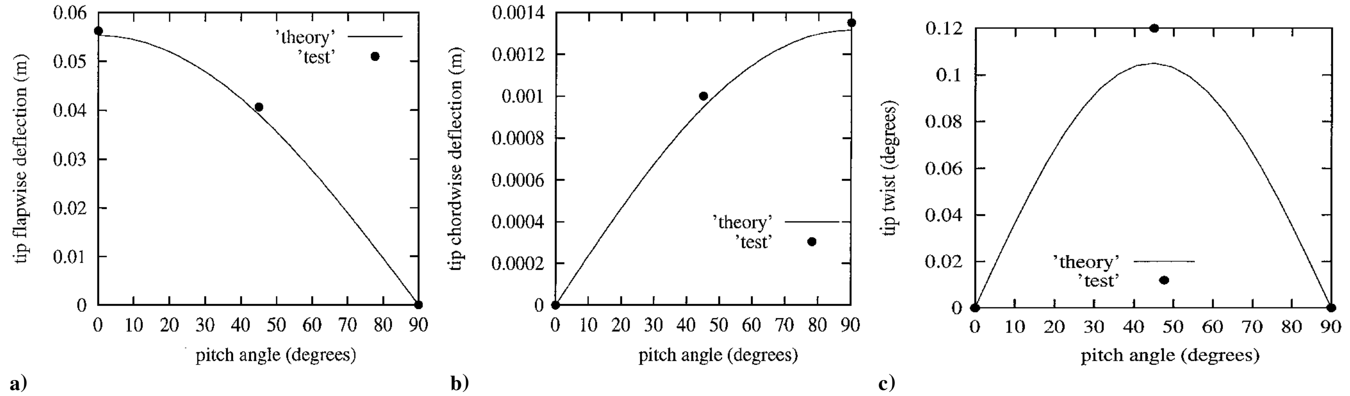

Fig. 3 At tip vs pitch angle: a) static flap b) chordwise bending deflections, and c) tip twist, gravity loading only.

where the structural mode number is $j = 1, 2, \ldots, N$ and the aerodynamic section number along the span of the wing is $l = 1, 2, \ldots, NN$. Using the Galerkin method, one obtains a set of state-space matrix equations from Eqs. (1–4) and (10–13):

$$[\mathcal{A}]\{\dot{q}\} + [\mathcal{B}]\{q\} = \{F_0\} + \{F_N\} \tag{14}$$

Note that the coefficient matrices $[\mathcal{A}]$ and $[\mathcal{B}]$ are dependent on the flow and structural parameters. The force vectors $\{F_0\}$ and $\{F_N\}$ are static force obtained from the effects of gravity and the nonlinear forces obtained from the structural nonlinearity and stall aerodynamics, respectively.

Equation (14) is the set of nonlinear equations of motion. A strictly linear flutter boundary is determined with Eq. (14) by setting $\{F_N\} \equiv 0$ and $\{F_0\} = 0$. There is no effect on the strictly linear flutter boundary of a preflutter static deflection or initial conditions. For $\{F_N\} \neq 0$ and a large static preflutter deformation, a dynamic perturbation approach is used to determine the small perturbation flutter boundary of this nonlinear system about a nonlinear and nontrivial static equilibrium condition. That is, one assumes that

$$\{q\} = \{\bar{q}\} + \{\hat{q}\} \tag{15}$$

where $\{\bar{q}\}$ represents the static equilibrium state variables and the corresponding quantities with a carat are the small (linear) dynamic perturbations about the static equilibrium state.

When Eq. (15) is substituted into Eq. (14), a set of static equilibrium equations and dynamic perturbation equations is obtained. The static equilibrium equations comprise a set of nonlinear algebraic equations for the unknown state vector $\{\bar{q}\}$.

The dynamic perturbation equations about a static equilibrium state are

$$[\bar{\mathcal{A}}]\{\dot{\hat{q}}\} + [\bar{\mathcal{B}}]\{\hat{q}\} = \{0\} \tag{16}$$

Note that the coefficient matrices $[\bar{\mathcal{A}}]$ and $[\bar{\mathcal{B}}]$ are dependent on the flow velocity and the static equilibrium state, for example, U, $\{\bar{q}\}$, etc.

To determine the dynamic nonlinear response of this aeroelastic system, we can use Eq. (14) and a time-marching approach.

A note on the sign convention may be helpful here. Vertical bending deflection w and the direction of gravity are taken as positive up, chordwise bending deflection v is taken as positive aft, and the torsional deflection and angle of attack are taken positive nose up. Note that because gravity is positive up, we are flying the wing upside down and, for example, a negative angle of attack is required to provide a lift downward to balance the wing weight.

Correlation Between Theory and Experiment

Static Deflections and Natural Frequencies Under Gravity Loading

The root mechanism of the experimental wing model is mounted to a very heavy support frame, which is attached to the ground. The root support mechanism allows the model to have a prescribed angle of attack or pitch of $\theta_0 = 0 \rightarrow 90$ deg. For assessing the static flap and chordwise bending deflections and twist at tip vs θ_0 under gravity loading only, three special pitch angles are considered, that is, $\theta_0 = 0$, 45, and 90 deg. The data are determined by directly measuring the difference between the undeformed and deformed tip position. The theoretical results are obtained from Eqs. (1–3) when the aerodynamic terms are set to zero. We use a time-marching approach to solve Eqs. (1–3) and to determine the steady solution, that is, the static deflections. The wing structural modes retained in the analysis were one chordwise mode, four flap modes, and one torsional mode. Preliminary calculations with various modal combinations verified that good convergence is achieved with these modes in the analysis. The results are shown in Figs. 3a–3c for the tip flap (Fig. 3a) and chordwise (Fig. 3b) bending deflections and tip twist (Fig. 3c) vs pitch angle. The solid line indicates the theoretical results, and the symbols • are from experiment. The agreement for the flap and chordwise deflections is excellent and for the twist is reasonably good.

The natural frequencies are determined by measuring the transfer function of input force and output root strain or acceleration. A force transducer B&K 8200 fixed near the wing root is excited by a minishaker B&K 4810 and a power amplifier B&K 2706. A four-channel signal analyzer (SD 380) provides a sweeping sinusoidal signal. The output signals from strain gauges (flap bending and torsion) and a microaccelerometer (chordwise) are inputs to the SD380 for transfer function analysis.

The theoretical results are obtained in terms from an eigenanalysis of the dynamic perturbation equation (16) when the aerodynamic terms are set to zero. The static equilibrium positions are determined by use of the time-marching approach, Eqs. (1–3). The results are shown in Figs. 4a–4c for the fundamental natural frequency vs pitch angle of attack. Figure 4a is for flap, Fig. 4b for chordwise bending deflections, and Fig. 4c for torsion. Of course, these motions are coupled, in general. The solid line indicates the theoretical results, and the symbols • are from experiment. The agreement for the chordwise frequency is excellent and for the flap and twist is reasonably good. The flap frequency has a slight change of $\theta_0 = 0 \rightarrow 90$ deg experimentally. The chordwise frequency decreases as θ_0 decreases from 90 to 0 deg, whereas the torsion frequency increases.

A correlation study was also conducted using previous experimental data reported by Dowell et al.[5] The results are included in the Appendix.

In general, good theoretical/experimental agreement is found. Indeed, it is somewhat better than that found in Ref. 5.

Static Aeroelastic Deflections of the Wing

We use a mirror deflection technique to measure the tip static aeroelastic deflections of the wing. A point determined by a reflected light source is marked on a readout grid paper placed on the top of the wind tunnel when the wing is undeflected. The readout grid paper is calibrated in the tip flap and twist deflections before the test. The reflected light source point with wing deflection as marked on the readout paper is then determined as the flow velocity is varied.

The theoretical results are obtained from Eq. (14) with the time-marching approach. The flow velocity is below the flutter velocity for these measurements and calculations. The wing is divided into 10 spanwise aerodynamic sections, that is, $NN = 10$. The

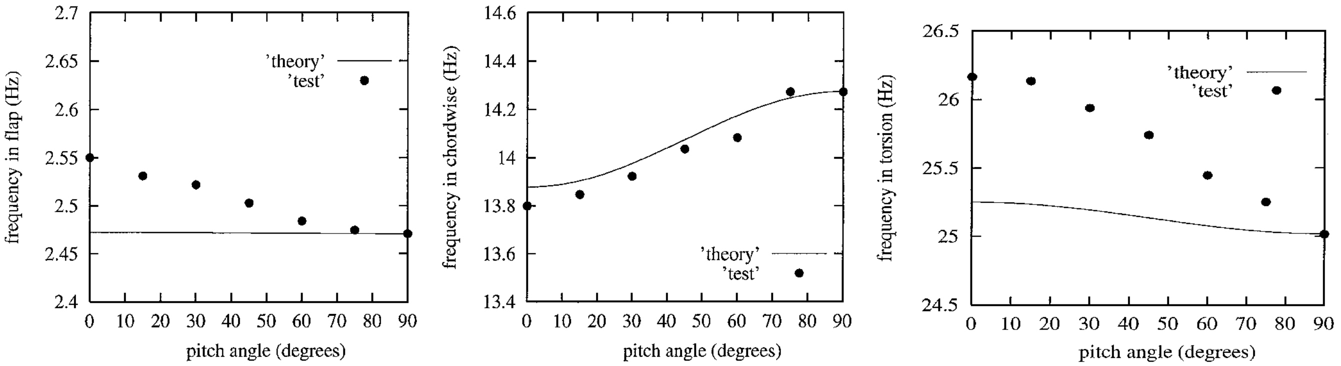

a) Flap **b) Chordwise bending** **c) Chordwise torsion**

Fig. 4 Fundamental natural frequency vs pitch angle.

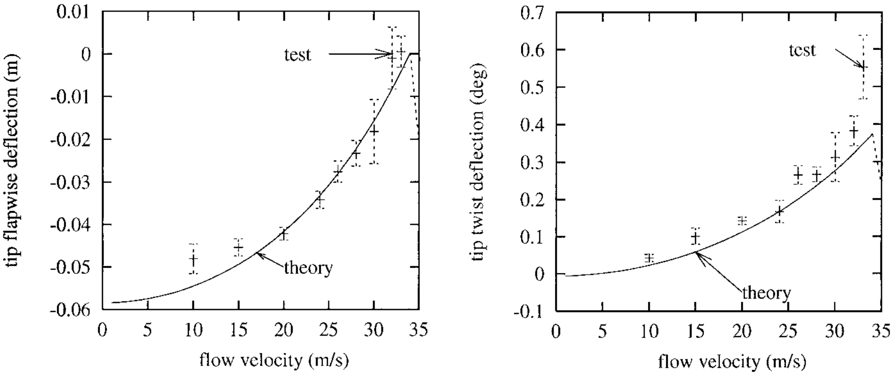

a) Flap **b) Twist**

Fig. 5 Static aeroelastic deflections of the wing vs flow velocity for pitch angle of attack $\theta_0 = 1$ deg.

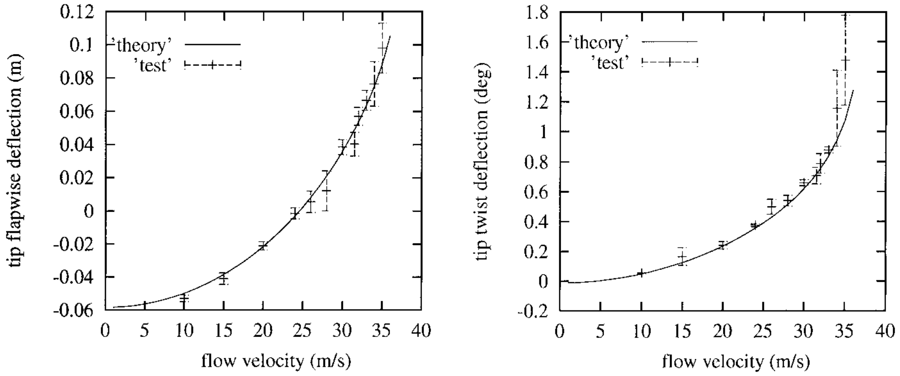

a) Flap **b) Twist**

Fig. 6 Static aeroelastic deflections of the wing vs flow velocity for pitch angle of attack $\theta_0 = 2.2$ deg.

stall aerodynamic data for an NACA 0012 airfoil are used in this paper.[7]

The theoretical and experimental results are shown in Figs. 5a and 5b for a steady angle of attack, $\theta_0 = 1$ deg. Figure 5a is for the tip flapwise deflection and Fig. 5b for the tip twist. The solid line indicates the theoretical results and the bar indicates the measured data. The experimental data appear have some scatter due to the turbulent aerodynamic noise, although the noise is small. A very high measurement sensitivity is obtained from the mirror technique. We use a bar in Fig. 5 to indicate the magnitude of the response uncertainty. As shown in Fig. 5, both the tip and twist deflection increase with increasing flow velocity, but the tip deflection is always negative until the flow velocity reaches 34.5 m/s. At that velocity, the aerodynamic forces provide sufficient lift to overcome the effect of gravity. At $U = 34.5$ m/s, the system enters into the flutter instability range. The consequent LCO has a certain nonzero mean or temporal average, and this is shown by a dashed line in Fig. 5. Also with LCO, aerodynamic stall occurs, and the lift coefficient C_l suddenly decreases. The measured data in Fig. 5 are acquired before the onset of flutter and LCO. The experimental LCO data will be discussed in the next section. The experimental data fall near the theoretical curves in Fig. 5. In general, the agreement is good except for some points at $U = 10$ and 15 m/s. In the higher flow velocity range, the data fluctuation increases due to greater aerodynamic turbulence.

Figure 6 shows the static aeroelastic deflections at the tip for $\theta_0 = 2.2$ deg. The balance between aerodynamic forces and the effect of gravity now occurs at $U = 25$ m/s. Compared to the results for $\theta_0 = 1$ deg (Fig. 5), a similar result is obtained, but the magnitude of the static aeroelastic deflections is larger than those for the $\theta_0 = 1$ deg, and a better agreement between experiment and theory is found.

Flutter and LCO Response

Very clear flutter and LCO responses are observed in the present wind-tunnel test. Flutter and LCO responses are determined for seven different steady angles of attack, that is, $\theta_0 = 0.25$, 0.5, 0.7,

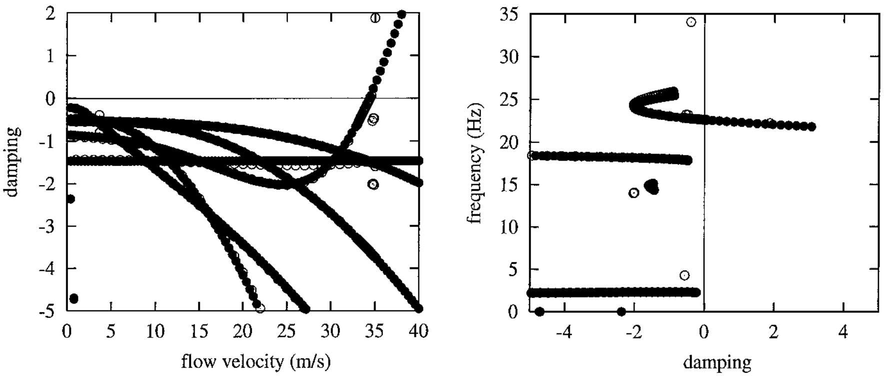

a) For real part **b) For root locus**

Fig. 7 Perturbation eigenvalue solution of the nonlinear aeroelastic system for $\theta_0 = 1$ deg.

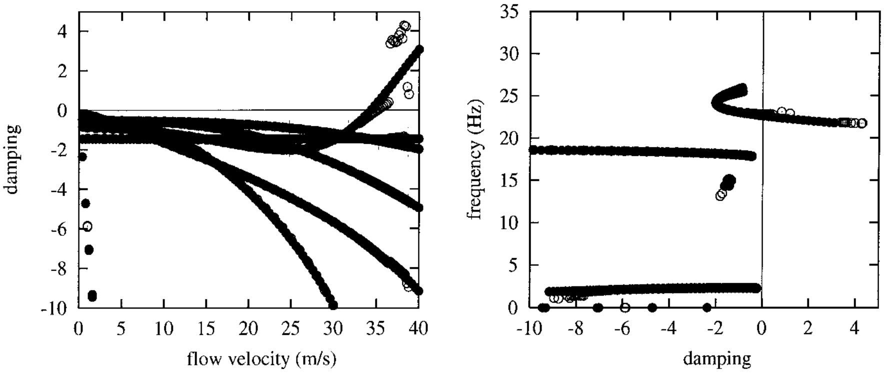

a) For real part **b) For root locus**

Fig. 8 Perturbation eigenvalue solution of the nonlinear aeroelastic system for $\theta_0 = 1.7$ deg.

1.0, 1.2, 1.5, and 1.7 deg. For the safety of this wing model, we did not determine flutter or LCO in the range of $\theta_0 \leq 0$ deg or $\theta_0 \geq 2$ deg.

The theoretical results are obtained from the dynamic perturbation equation (16) and also with a time-marching approach for the full nonlinear equations (14). For no static wing deformation, the strictly linear flutter speed and frequency are found to be 34.4 m/s and 22.57 Hz, respectively. In this case, we considered the effects of the tip slender body aerodynamics on flutter. The results are $U_f = 34.2$ m/s and $\omega_f = 22.44$ Hz without tip slender body aerodynamics included. The effect of the tip body aerodynamics is, thus, seen to be small.

Figures 7a and 7b show a graphical representation of the perturbation equations' eigenanalysis in the form of real eigenvalues $\mathrm{Re}(\lambda_i)$ (damping) vs the flow velocity and also a root locus plot (frequency vs damping) as indicated by the symbol ○. There is an intersection of $\mathrm{Re}(\lambda_i)$ with the velocity axis at $U_f = 34.5$ m/s, and the corresponding flutter oscillatory frequency is $\omega_f = 22.59$ Hz for $\theta_0 = 1$ deg. For no static wing deformation, the strictly linear flutter results are also shown in Fig. 7 as indicated by the symbol •. The two results are almost the same. The reason can be explained by Fig. 5a. Here, the static tip deflection approaches zero when the system is near the flutter velocity. The effects of the geometric structural nonlinearity thus become small near the flutter condition.

Similar to the preceding results, Figs. 8a and 8b show the eigenanalysis for $\theta_0 = 1.7$ deg. The flutter velocity is $U_f = 35.2$ m/s and the corresponding flutter oscillatory frequency is $\omega_f = 2.8$ Hz. The flutter velocity and frequency increase 2.3 and 1% as compared to the strictly linear results. In this case, we find the tip deflection is 0.05 m when $U = 35.2$ m/s. The effects of the structural nonlinearity are to increase the stability. From Fig. 4c, it is seen that the natural torsional frequency of the wing model increases as the tip deflection increases.

The effects of the structural nonlinearity depend on the bending stiffness ratio of EI_2/EI_1. In Ref. 3, it is shown that the angle of twist and the ratio of the flapwise deflection to wingspan vary as the square root of EI_1/EI_2 for the LCO amplitude and/or the initial disturbance required to initiate LCO. For the present wing model, EI_2/EI_1 is only 44.05, which is much lower than the wing model used in Refs. 2 and 3 ($EI_2/EI_1 = 200$). Thus, the nonlinear effects should be weaker, that is, the LCO amplitude or the initial disturbance required to initiate LCO is larger for larger EI_1/EI_2 or smaller EI_2/EI_1.

Figure 9 shows the dynamic perturbation flutter velocity (Fig. 9a) and frequency (Fig. 9b) vs the pitch angle of attack from both theory and experiment. The solid line is for the dynamic perturbation solution, and the symbol • is for the experimental data (onset velocity of flutter or LCO). For comparison, the linear flutter solution is also plotted in Fig. 9, as shown by the broken line. The linear flutter solution is near the minimum flutter velocity and is located at a pitch angle between $\theta_0 = 1$ and 1.2 deg. The maximum error between theory and experiment is only about 3%. The experimental flutter frequency is lower than those for the theory. The maximum error is about 5.4%.

Figure 10 shows the theoretical LCO time history of the midspan flapwise deflection (Fig. 10a) and the tip twist deflection (Fig. 10b) for $U = 35$ m/s and $\theta_0 = 1$ deg; from Fig. 10, we find the stall aerodynamic nonlinearity leads to an LCO.

Figure 11 shows a comparison between theoretical and experimental time histories and the corresponding fast Fourier transform (FFT) analysis for flapwise deflection at the midspan point for $U = 35$ m/s and $\theta_0 = 1$ deg. Figure 11a is the theoretical time history from $t = 29$ to 30 s, Fig. 11b is the measured time history, and Fig. 11c is the FFT analysis. The motion includes two dominant frequency components. One comprises 22.59 Hz from the theory and 21.4 Hz from the test, which corresponds to the flutter frequency. The other comprises 45 Hz from theory and 42 Hz from the test, which is close to the second harmonic of the flutter frequency. The response is dominated by the flutter frequency. The agreement between theory and experiment is reasonably good.

As shown in Fig. 7b, it is found that the flutter mode is dominated by the coupling between the first torsion mode and second flap mode. The LCO vibration mode shape is similar to the flutter mode.

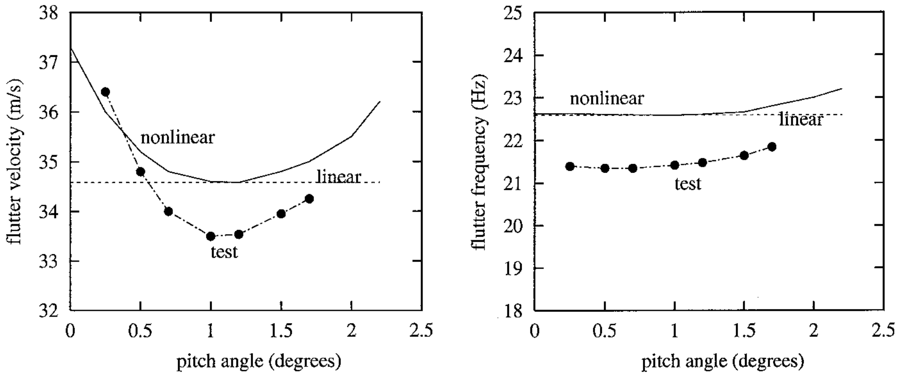

a) Flutter velocity **b) Flutter frequency**

Fig. 9 Perturbation eigenvalue solution of the nonlinear aeroelastic system vs pitch angle.

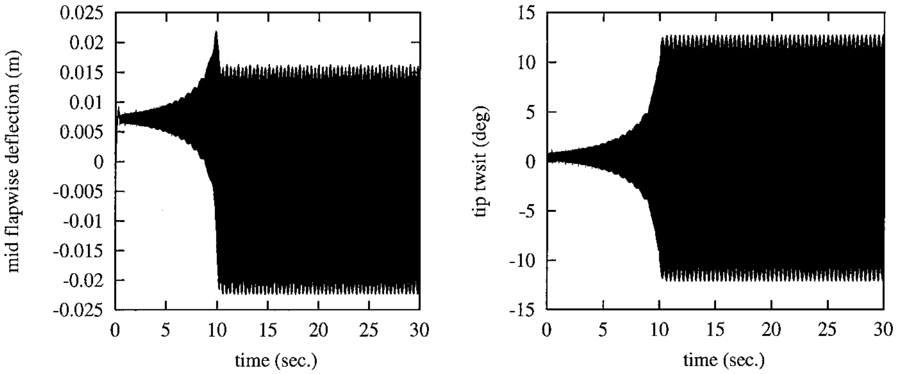

a) Midspan flapwise deflection **b) Tip twist**

Fig. 10 Time history for $U = 35$ m/s and $\theta_0 = 1$ deg.

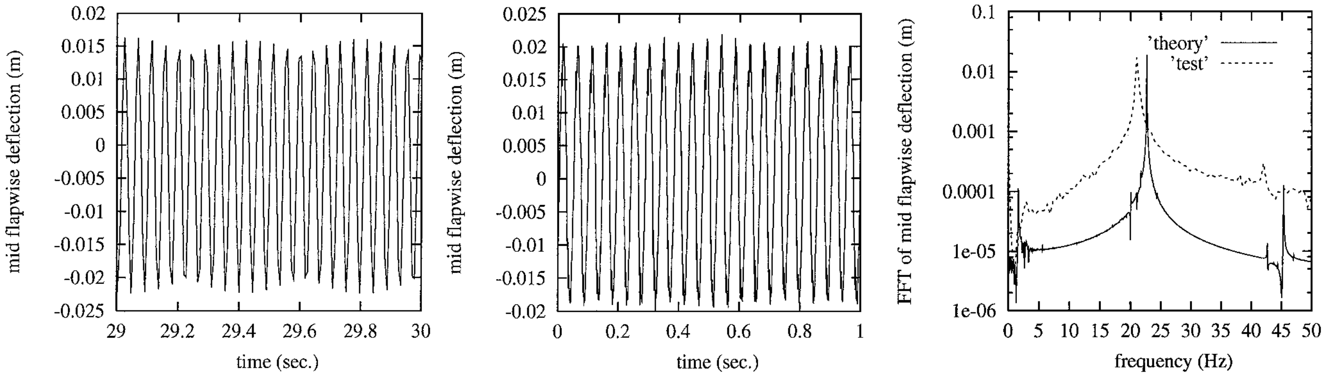

a) Theory **b) Measured data** **c) FFT analysis**

Fig. 11 Time history for $U = 35$ m/s and $\theta_0 = 1$ deg, midspan flapwise deflection.

Figure 12 shows the theoretical LCO mode shape for $U = 35$ m/s and $\theta_0 = 1$ deg. This LCO mode shape is also observed in the wind-tunnel test and has been recorded on video tape. The experimental data point at the midspan is also plotted on Fig. 12.

When the flow velocity is high, the theoretical LCO response appears as a beat oscillation, but this was not observed in the test. As an example, Fig. 13a shows the theoretical time history and Fig. 13b shows the corresponding FFT analysis for $U = 38$ m/s and $\theta_0 = 1$ deg. The very close frequencies are 20.96 and 22.63 Hz, which are both important for the response. However, 22.63 Hz seems more significant.

Other interesting results are the phase plane plots of the motion at the wing tip. We use the mirror deflection technique to measure the twist deflection and flapwise bending slope for $U = 35$ m/s and $\theta_0 = 1$ deg. Figure 14a shows the theoretical results and Fig. 14b shows the test results. The grid paper is calibrated. In Fig. 14b, each square grid corresponds to 1 deg by 1 deg. The two results show reasonably good agreement.

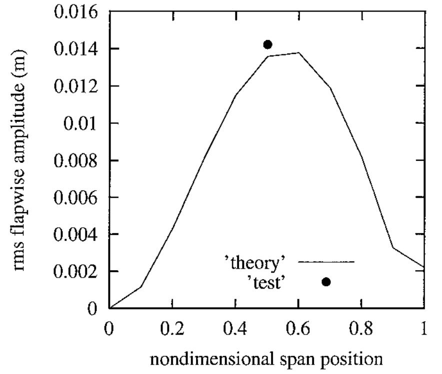

Fig. 12 LCO vibration mode shape for $U = 35$ m/s and $\theta_0 = 1$ deg.

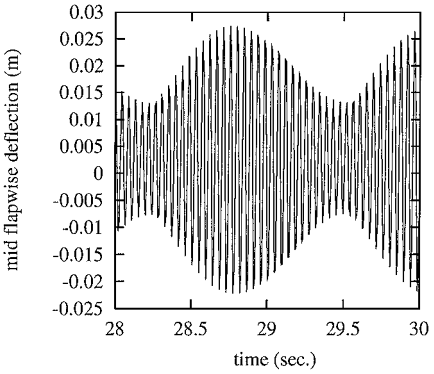

Fig. 13a Time history for $U = 38$ m/s and $\theta_0 = 1$ deg.

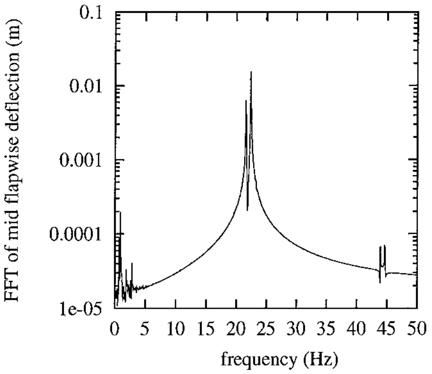

Fig. 13b FFT analysis for $U = 38$ m/s and $\theta_0 = 1$ deg.

A typical LCO amplitude and LCO frequency vs flow velocity for $\theta_0 = 1$ deg and at the midspan position are shown in Figs. 15a and 15b, respectively. The theoretical and experimental amplitudes are taken as rms average values from a 50-s sampling interval. The symbols ○ and ● indicate the experimental results for increasing and decreasing flow velocity, respectively. The solid and broken lines (without symbols) indicate the theoretical results for increasing and decreasing flow velocity, respectively. The symbol △ indicates the linear flutter velocity, which is calculated from the perturbation eigenvalue solution. For the increasing flow velocity case, the theoretical LCO occurs when the flow velocity is larger than the perturbation flutter velocity and the amplitude has a jump from almost rest to a larger value. Once the onset of LCO occurs, the amplitude increases smoothly with an increase in the flow velocity. When $U > 38.6$ m/s, a numerical or possibly a physical divergence is found in the theoretical model. For the case of decreasing flow velocity, as shown by the broken line, the LCO amplitude decreases but does not exactly coincide with those for the increasing velocity case. Also, there is a jump in the LCO response at $U = 33.5$ m/s, which is a distinctly lower velocity than that found for the increasing velocity case, that is, $U = 34.5$ m/s.

To show further details of the theoretical results, we use two time history figures to show the LCO responses obtained from the increasing and decreasing flow velocity processes. The results are shown in Figs. 16a and 16b for $\theta_0 = 1$ deg. Figure 16a is the result from increasing velocity and Fig. 16b is for decreasing velocity. There are 11 flow velocities from $U = 33$ to 38 m/s, with $\Delta U = 0.5$ m/s considered in the calculation. At each flow velocity, the time history is computed until the system achieves a steady-state LCO response. In general, it takes about 20 s (a time step of $\Delta t = 1/2048$ s is used). The LCO response for the last 1 s is shown in Fig. 16a, that is, the LCO response is shown in time intervals of 1 s for the several flow velocities. For the next flow velocity (increasing ΔU), we use initial conditions that are provided by the preceding LCO state. This process is continuous in time until the flow velocity increases

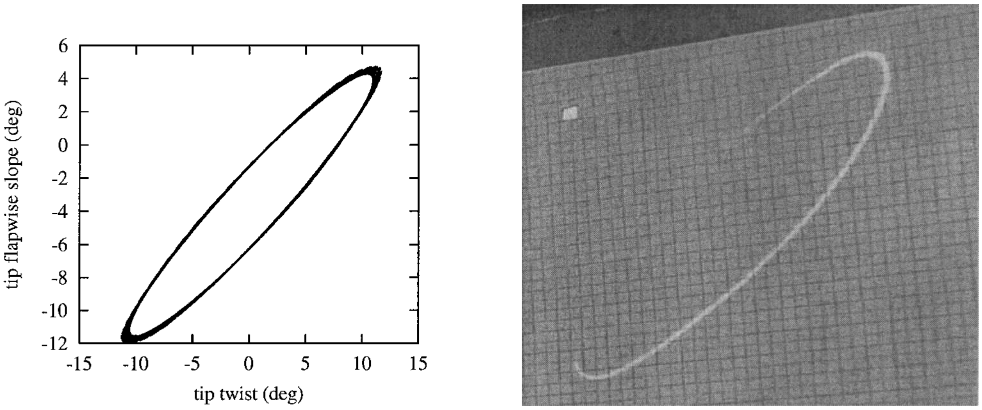

a) Theory **b) Test**

Fig. 14 Phase plane plot of tip flapwise bending slope vs twist for $U = 35$ m/s and $\theta_0 = 1$ deg.

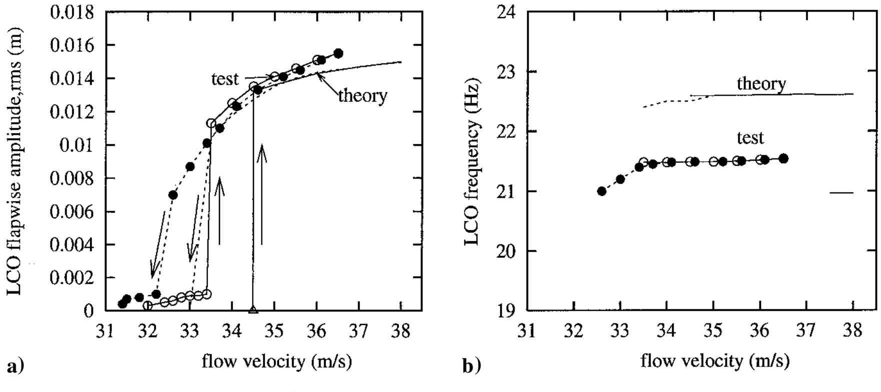

Fig. 15 Midspan LCO: a) amplitude and b) frequency vs flow velocity for $\theta_0 = 1$ deg.

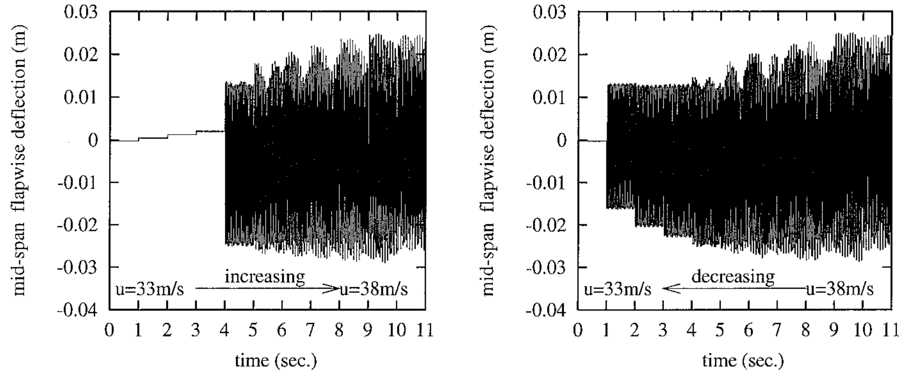

a) Increasing flow velocity process **b) Decreasing process for $\theta_0 = 1$ deg**

Fig. 16 LCO time history at midspan.

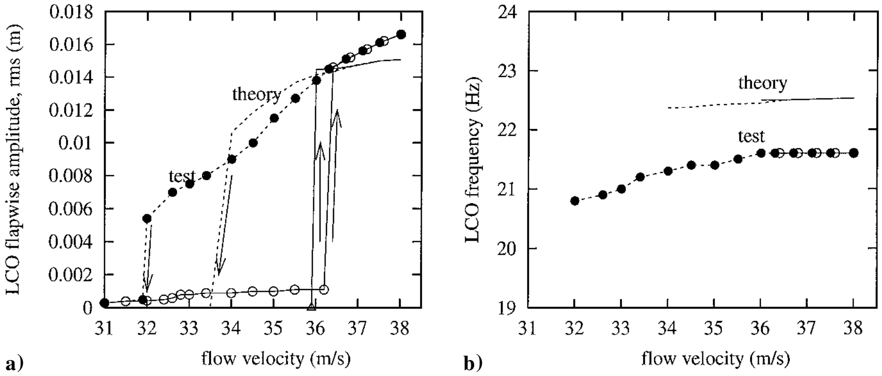

Fig. 17 Midspan LCO: a) amplitude and b) frequency vs flow velocity for $\theta_0 = 0.25$ deg.

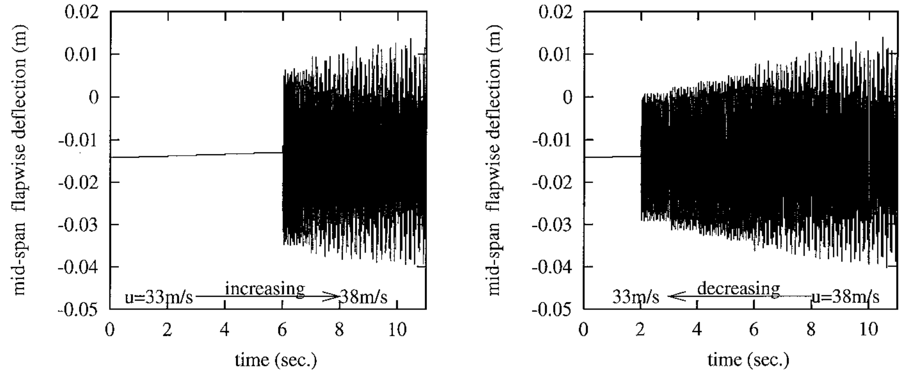

a) Increasing flow velocity process **b) Decreasing process for $\theta_0 = 0.25$ deg**

Fig. 18 LCO time history at midspan.

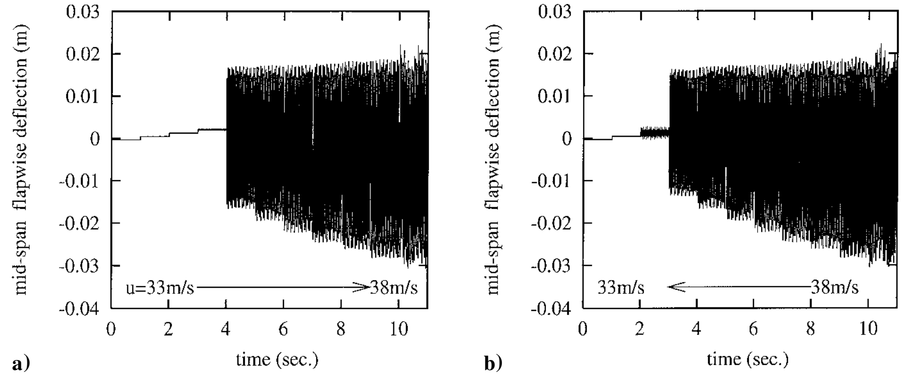

Fig. 19 LCO time history at midspan: a) increasing flow velocity process and b) decreasing process for $\theta_0 = 1$ deg and the structural nonlinearity removed.

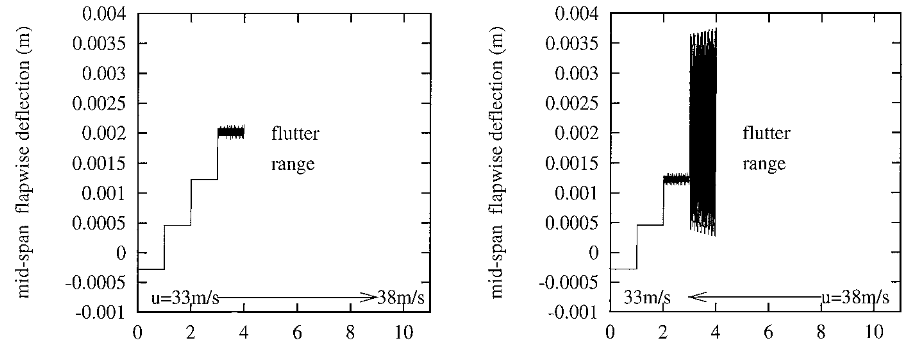

a) b)

Fig. 20 LCO time history at midspan: a) increasing flow velocity process and b) decreasing process for $\theta_0 = 1$ deg and the stall aerodynamic nonlinearity removed.

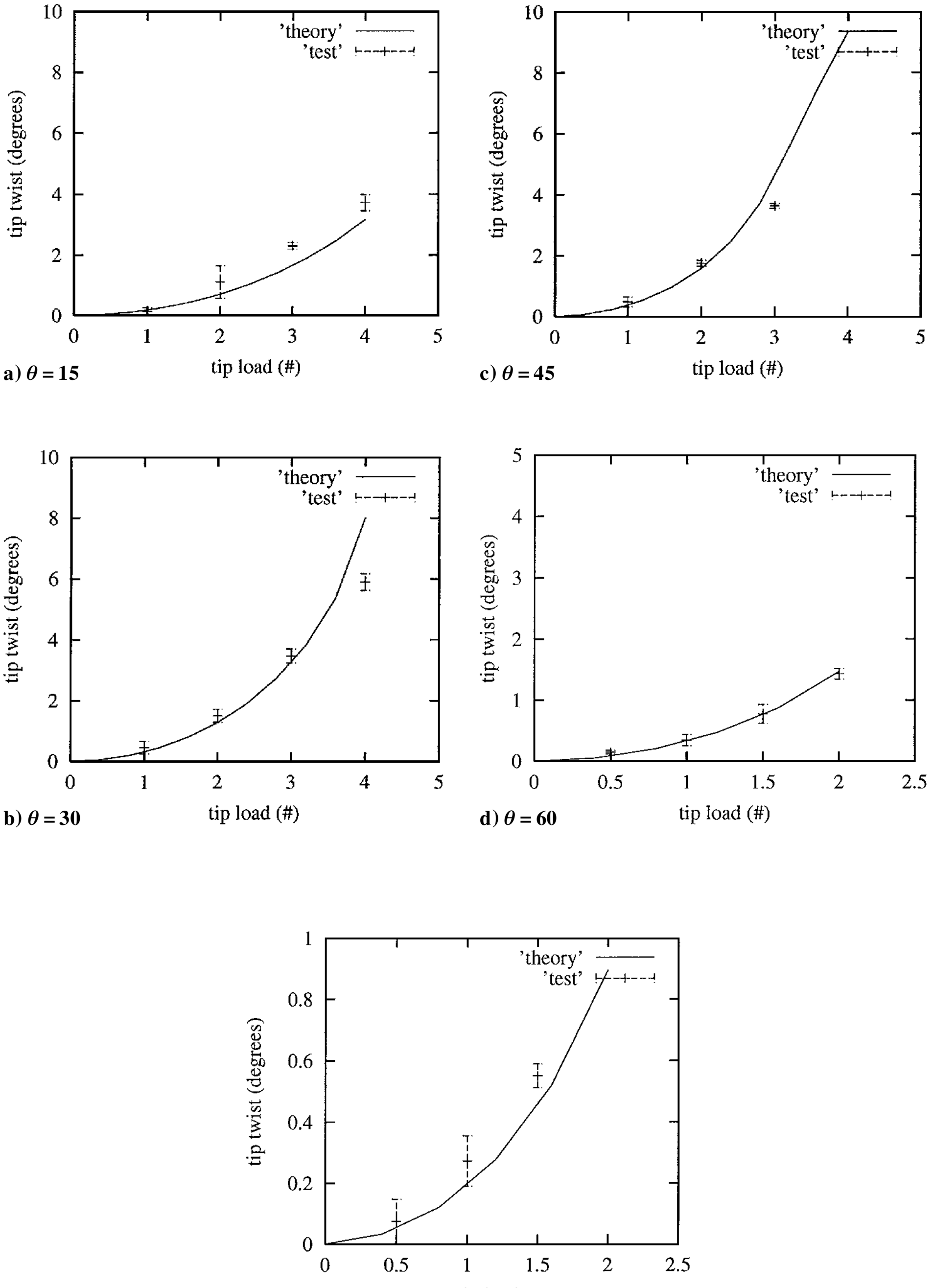

a) $\theta = 15$

c) $\theta = 45$

b) $\theta = 30$

d) $\theta = 60$

e) $\theta = 75$ deg

Fig. A1 Static twist vs load.

to $U = 38$ m/s. For the decreasing velocity process, the results are shown in Fig. 16b. The process method is the same as the preceding method. Again, we see hysteresis in the response depending on whether the flow velocity is increasing or decreasing.

For the experimental measurement, we also observed two different LCO responses for increasing and decreasing flow velocity. With increasing flow velocity, we find a jump at $U = 33.5$ m/s, which is similar to the theoretical results at $U = 34.5$ m/s as shown by the symbol ○ with a solid line. This jump velocity is called the experimental flutter velocity. As the flow velocity increases further, the LCO amplitude measured has a modestly larger increase than that found from theory. For model safety, the test was stopped at $U = 36.5$ m/s. When the flow velocity is decreased, we find another jump at $U = 32.4$ m/s as shown in Fig. 16a and as indicated by the symbol ● with a broken line. The experimental LCO amplitudes for decreasing velocity are modestly smaller than those found for increasing velocity.

The LCO frequency vs flow velocity is shown in Fig. 15b. The symbols used in Fig. 15b are the same as for Fig. 15a. As shown in Fig. 15b, the LCO frequency has a slight change as the flow velocity increases. At high velocity, the theoretical LCO has two close frequencies as discussed earlier in regard to Fig. 13. The theoretical/experimental agreement is reasonably good.

The theoretical/experimental results for LCO amplitude and frequency vs flow velocity for $\theta_0 = 0.25$ deg and at the midspan position are shown in Figs. 17a and 17b. The theoretical LCO time histories obtained from the increasing and decreasing flow velocity

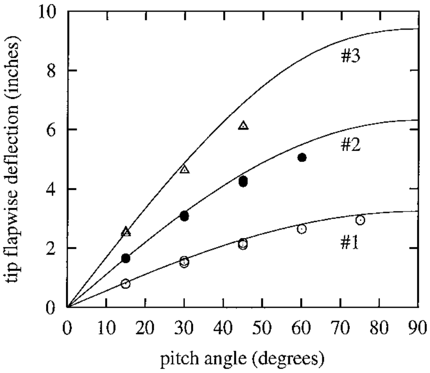

Fig. A2 Static tip flapwise deflection vs pitch angle, various load: solid line, theory; symbols, experiment: △, $P = 3$; ●, $P = 2$; and ○, $P = 1$.

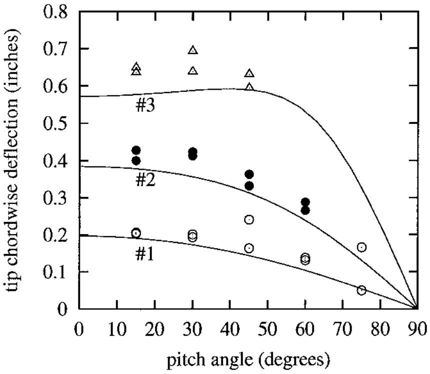

Fig. A3 Static tip chordwise deflection vs pitch angle, various load: solid line, theory; symbols, experiment: △, $P = 3$; ●, $P = 2$; and ○, $P = 1$.

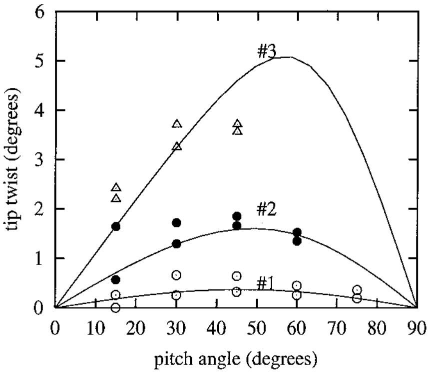

Fig. A4 Static tip twist deflection vs pitch angle, various load: solid line, theory; symbols, experiment: △, $P = 3$; ●, $P = 2$; and ○, $P = 1$.

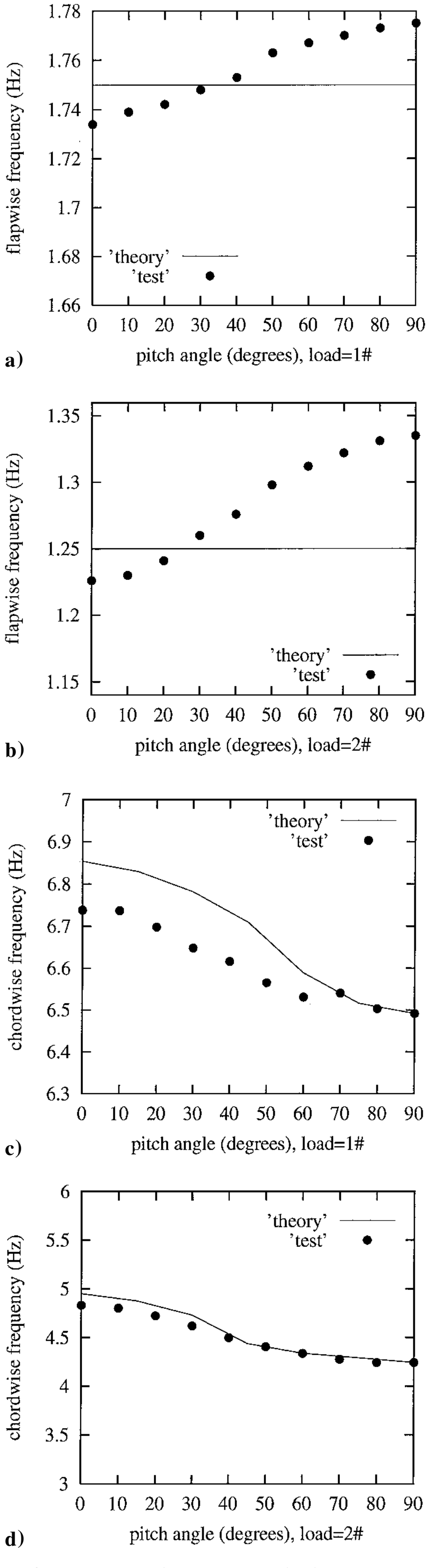

Fig. A5 Flap frequency vs pitch angle: solid line, theory and ●, experiment: a) $P = 1$; b) $P = 2$, chordwise frequency vs pitch angle; c) $P = 1$; and d) $P = 2$.

processes are shown in Figs. 18a and 18b. For the other pitch angles of attack, the experimental/theoretical results are very similar to those for $\theta_0 = 1$ and 0.25 deg.

A hysteresis phenomenon was found from both the theoretical prediction and experimental observation. To determine the source of the hysteresis, the theoretical calculation was repeated with the structural nonlinearity or the stall aerodynamic nonlinearity removed, alternatively. The results are shown in Figs. 19 and 20 for $\theta_0 = 1.0$ deg. It is found that the structural nonlinearity does not lead the hysteresis and LCO as shown in Fig. 19; however, the stall aerodynamic nonlinearity is responsible for this hysteresis and LCO behavior as shown in Fig. 20.

Conclusions

The present experimental and theoretical results provide new insights into nonlinear aeroelastic phenomena for high-aspect-ratio wings (with a tip slender body) that have a beam-like structural behavior. The effects of the geometric structural nonlinearity of the beam theory and aerodynamic stall on both the flutter instability boundary and the nonlinear response have been studied. The effects of the geometric structural nonlinearity depend on the ratio of the flap and chordwise bending stiffnesses, EI_2/EI_1. For relatively small EI_2/EI_1, the flutter instability boundary has only a small change due to the structural nonlinearity and preflutter static deformation. The onset of an LCO is dependent on a delicate balance between stall aerodynamics and the structural nonlinear forces.[2,3] However, the stall aerodynamics are dominant for the present experimental wing model.

Appendix: Static Deflections and Natural Frequencies Under Gravity Load

A further assessment of the present calculation method, a correlation study was made with the experimental data of Ref. 5. The results are shown here in Figs. A1–A5, which correspond to Figs. 4–8 in Ref. 5. For ease of comparison, the same notation is used in this Appendix as in Ref. 5. Generally, good agreement between theory and experiment is found.

Acknowledgments

This work was supported by the Defense Advanced Research Projects Agency through Air Force Office of Scientific Research Grant F49620-99-1-00253, "Aeroelastic Leveraging and Control Through Adaptive Structures," under the direction of Ephrahim Garcia and Dan Segalman. We would also like to thank our colleage Robert Clark for useful discussion of this work and graduate student Emil Ardelean for his assistance. All numerical calculations were done on a supercomputer, T916, in the North Carolina Supercomputing Center.

References

[1] Hodges, D. H., and Dowell, E. H., "Nonlinear Equations of Motion for the Elastic Bending and Torsion of Twisted Nonuniform Rotor Blades," NASA TN D-7818, 1974.

[2] Patil, M. J., Hodges, D. H., and Cesnik, C. E. S., "Limit Cycle Oscillations in High-Aspect-Ratio Wings," AIAA Paper 99-1464, 1999.

[3] Tang, D. M., and Dowell, E. H., "Effects of Geometric Structural Nonlinearity on Flutter and Limit Cycle Oscillations of High-Aspect Ratio Wings," *Journal of Fluids and Structures* (submitted for publication).

[4] Tran, C. T., and Petot, D., "Semi-Empirical Model for the Dynamic Stall of Airfoils in View to the Application to the Calculation of Responses of a Helicopter Blade in Forward Flight," *Vertica*, Vol. 5, No. 1, 1981, pp. 35–53.

[5] Dowell, E. H., Traybar, J., and Hodges, D. H., "An Experimental–Theoretical Correlation Study of Non-Linear Bending and Torsion Deformations of a Cantilever Beam," *Journal of Sound and Vibration,* Vol. 55, No. 4, 1977, pp. 533–544.

[6] Patil, M. J., Hodges, D. H., and Cesnik, C. E. S., "Nonlinear Aeroelasticity and Flight Dynamics of High-Altitude Long-Endurance Aircraft," AIAA Paper 99-1470, 1999.

[7] Patil, M. J., and Hodges, D. H., "On the Importance of Aerodynamic and Structural Geometrical Nonlinearities on Aeroelastic Behavior of High-Aspect-Ratio Wings," AIAA Paper 2000-1448, 2000.

[8] Minguet, P., and Dugundji, J., "Experiments and Analysis for Composite Blades Under Large Deflections, Part II: Dynamic Behavior," *AIAA Journal*, Vol. 28, No. 9, 1990, pp. 1580–1588.

[9] Bisplinghoff, R. L., Ashley, H., and Halfman, R. L., *Aeroelasticity*, Addison Wesley Longman, Reading, MA, 1955, pp. 418–420.

E. Livne
Associate Editor